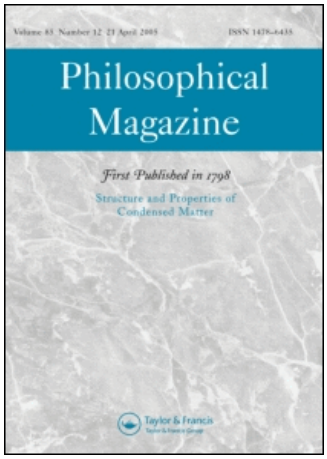

Philosophical Magazine
First published in 1798
Publication details, including instructions for authors and subscription information:
http://www.informaworld.com/smpp/title~content=t713695589

Formation mechanism of nanostructures in austenitic stainless steel during equal channel angular pressing

C. X. Huang [a]; G. Yang [b]; B. Deng [b]; S. D. Wu [a]; S. X. Li [a]; Z. F. Zhang [a]
[a] Shenyang National Laboratory for Materials Science, Institute of Metal Research, Chinese Academy of Sciences, Shenyang, 110016, China
[b] Central Iron and Steel Research Institute, Beijing, 100081, China

Online Publication Date: 01 November 2007
To cite this Article: Huang, C. X., Yang, G., Deng, B., Wu, S. D., Li, S. X. and Zhang, Z. F. (2007) 'Formation mechanism of nanostructures in austenitic stainless steel during equal channel angular pressing', Philosophical Magazine, 87:31, 4949 - 4971
To link to this article: DOI: 10.1080/14786430701594046
URL: http://dx.doi.org/10.1080/14786430701594046

Philosophical Magazine,
Vol. 87, No. 31, 1 November 2007, 4949–4971

Formation mechanism of nanostructures in austenitic stainless steel during equal channel angular pressing

C. X. HUANG*†, G. YANG‡, B. DENG‡, S. D. WU†,
S. X. LI† and Z. F. ZHANG*†

†Shenyang National Laboratory for Materials Science, Institute of Metal Research,
Chinese Academy of Sciences, Shenyang 110016, China
‡Central Iron and Steel Research Institute, Beijing, 100081, China

(*Received 15 March 2007; accepted in revised form 20 July 2007*)

An ultra-low carbon austenitic stainless steel was successfully pressed from one to eight passes by equal channel angular pressing (ECAP) at room temperature. By using X-ray diffraction, optical microscopy and transmission electron microscopy, the microstructural evolution during ECAP was investigated to reveal the formation mechanism of strain-induced nanostructures. The refinement mechanism involved the formation of shear bands and deformation twins, followed by the fragmentation of twin lamellae, as well as successive martensite transformation from parent austenitic grains with sizes ranging from microns to nanometres through the processes $\gamma(\text{fcc}) \rightarrow \varepsilon(\text{hcp}) \rightarrow \alpha'(\text{bcc})$. After pressing for eight passes, two types of nanocrystalline grains were achieved: (a) nanocrystalline austenite with a mean grain size of ~31 nm and (b) strain-induced nanocrystalline α'-martensite with a size of ~74 nm. The formation mechanisms are discussed in terms of microstructural subdivision via deformation twinning and martensite transformation.

1. Introduction

Extensive investigations of ultrafine-grained (UFG, grain size $d < 1\,\mu\text{m}$) and nanocrystalline (grain size $d < 100\,\text{nm}$) materials show that they exhibit superior mechanical properties, such as high strength, which can coexist with good ductility [1–3]. Many methods have been developed for producing UFG and nanocrystalline materials in recent years. Among those methods, severe plastic deformation (SPD) is the most important one that decomposes the microstructure of coarse grains into UFG or nanocrystalline microstructures without introducing porosity or impurities [4]. Typical SPD techniques include high-pressure torsion (HPT), equal channel angular pressing (ECAP), surface mechanical attrition treatment (SMAT) and accumulative roll-bonding [5–7], etc. Due to its unique capacity for producing bulk samples with sizes of centimetres, ECAP has received much attention during the past decade, and successfully applied for many metals, e.g. Al, Cu, Ni, Fe, Mg and Ti, as well as their alloys [7–17].

*Corresponding author. Email: chxhuang@imr.ac.cn; zhfzhang@imr.ac.cn

Philosophical Magazine
ISSN 1478–6435 print/ISSN 1478–6443 online © 2007 Taylor & Francis
http://www.tandf.co.uk/journals
DOI: 10.1080/14786430701594046

As far as the microstructural evolution during ECAP is concerned, the grain refinement generally originates from various dislocation activities in cubic metals and alloys with medium or high stacking fault energy (SFE), e.g. Al, Cu, Fe and their alloys [7–12]. With increasing strain, plastic-strain-induced dislocations arrange themselves into various dislocation configurations depending on the nature of the deformed materials, such as the geometrically necessary boundary, incidental dislocation boundary, dense dislocation wall, etc [7–12, 18]. Further straining leads these dislocation boundaries to evolve into high-angle grain boundaries (GBs), which subdivide the original grains to finer grains. The limiting grain size obtained via the dislocation subdivision mechanism is typically of the order of several hundred of nanometres (usually refers to UFG range), but not really of nanometre scale ($<$100 nm). For example, the minimum grain sizes obtained in Cu, Fe and low carbon steel are only of 200–300 nm [10–12]. Further pressing does not refine grains obviously but only increases the misorientation between adjacent grains [19]. This might be due to dynamic recovery that opposes the accumulation of dislocations and subdivision of grains on a finer scale [10, 19].

In addition to dislocation slip, deformation twinning is another important deformation mechanism related to grain refinement in fcc materials with low SFEs and in hcp materials. The refinement mechanism via deformation twinning has been identified in several hcp materials, such as Ti and Zr during the process of ECAP [20, 21]. For low-SFE fcc materials, texture evolution and the final grain microstructures processed by ECAP have been reported in Ag (22 mJ m^{-2} [22–24]) and Cu–30% Zn (20 mJ m^{-2} [17, 22]), respectively. However, there has been little investigation of the influence of deformation twinning upon grain refinement during ECAP. In contrast, the grain refinement process via deformation twinning has been revealed by other SPD methods. For instance, in Inconel 600 alloy (28 mJ m^{-2} [22]) and 304 stainless steel (SS, 21 mJ m^{-2} [22]), deformation twins and their interplays with dislocations dominate the grain refinement process during SMAT [25, 26]. Zhao *et al*. [27] recently confirmed that, due to the presence of large amounts of deformation twins, the grain sizes obtained by HPT could decrease from 75 nm in Cu to 17 nm in Cu–30% Zn.

As is well known, austenitic SS is one material with low SFE in which deformation twinning occurs readily under plastic straining [28]. An important characteristic of these materials is their sensitivity to deformation-induced martensite transformation (DIMT) under plastic deformation due to the energetic instability of the austenitic structure [29–31]. This suggests that a refinement mechanism via DIMT is possible in those materials susceptible to DIMT, such as austenitic steels and some shape-memory alloys. In the literature, several such evidences show that strain-induced martensite nanostructures can be created from the parent austenitic matrix. For example, Zhang *et al*. [26] reported that nanocrystalline α' martensite with size of several tens of nanometres was induced on the surface layer of 304 SS. They observed that α' martensite nucleated at the intersections of twins, but failed to give an explanation of how the parent austenite with micron-sized grains was transformed into nanocrystalline α' martensite in detail. In our recent research, we have confirmed that nanocrystalline α' martensite ($\sim$70 nm) was created from an austenitic SS during ECAP [32]. However, the formation mechanism of nanocrystalline martensite induced by plastic straining is not yet well understood. This gives rise

to several interesting questions. How does the martensite nucleate from the austenite? How does the austenite grain size affect martensite nucleation and its grain size, along with their contribution to the formation of nanocrystalline martensite? Thirdly, how to accommodate plastic straining of martensite itself and what is the contribution to the grain refinement? All these questions are very important for the formation of nanocrystalline martensite and will be examined in this paper through systematic observations on the microstructural evolution in an ultra-low carbon austenitic SS during ECAP. We will show that nanocrystalline austenite with a very fine grain size can also be obtained via deformation twinning and subsequent twin fragmentation during ECAP.

2. Experimental

The material used in this study is an ultra-low carbon austenitic SS (304L type) having a composition, in wt%, of 0.007 C, 18.46 Cr, 11.82 Ni, 1.61 Si, 0.008 S, 0.018P. 0.29 Mn and balance Fe. A hot-rolled billet was austenitized at 1150°C for 2 h. The initial rods for ECAP with a dimension of $\Phi 8 \times 45$ mm were cut from the annealed billet.

The ECAP procedure was performed using a split die made from a tool steel (AISI M4-like) [32] with two channels intersecting at an inner angle of 90° (Φ) and an outer angle of 30° (Ψ) [4]. Both the inlet and outlet channels had the same diameter of 8 mm. The outer corner radius was half the diameter of the channel. The rods coated with MoS_2 lubricant were pressed for one, two, four, six or eight passes at room temperature (RT). In order to avoid the instability of punch, the pressing speed was selected to be slow ($\sim$9 mm min^{-1}). Route Bc was adopted, i.e. the sample was rotated round its longitudinal axis by 90° clockwise before each pass. The average load was $\sim$110 kN and increased gradually to the maximum load of $\sim$140 kN with increasing passes. The equivalent von Mises strain for single pass is $\sim$1 [33].

A Rigaku D/max-2400 X-ray diffractometer (12 kW) with Cu-K_α radiation was used to determine the phase constitution. The volume fraction of retained austenite, V_γ, was calculated from the integrated intensity of the martensitic and austenitic peaks using the following equation [34, 35],

$$V_\gamma = \frac{1.4I_\gamma}{I_{\alpha'} + 1.4I_\gamma}, \tag{1}$$

where I_γ is the average integrated intensity obtained at the $(220)_\gamma$ and $(311)_\gamma$ peaks, and $I_{\alpha'}$ is that obtained at the $(211)_{\alpha'}$ peak.

The microstructure observations were performed by optical microscopy (OM) and JEM-2000FXII transmission electron microscope (TEM), operating at 200 kV. The samples for OM and TEM observations were cut from the centre of the pressed rod perpendicular to its longitudinal axis. For OM experiments, the specimens were ground and electrochemically polished in a solution of 10 g oxalic acid and 100 ml water at a voltage of 10 V. For TEM observations, thin foils

(~0.4 mm in thickness) were ground to ~40 μm thick, then thinned by the twin-jet polishing method in a solution of 10% perchloric acid and ethanol in a voltage range 18–22 V.

3. Experimental results

3.1. *X-ray diffraction analysis*

Figure 1a shows the X-ray diffraction (XRD) profiles of the initial samples and after ECAP (one, four and eight passes). It is evident that both austenitic (γ phase, fcc structure) and martensitic (α' phase, bcc structure) peaks can be seen in the XRD profiles of the post-ECAP samples. Besides, the (101) diffraction peak of ε phase (hcp structure) is also detected in the one-pass sample, as indicated by the inverse triangle in the inset. With increasing strain, the intensity of the ε peak decreases gradually and becomes negligible after six passes. Apparently, the DIMT via $\gamma \rightarrow (\varepsilon) \rightarrow \alpha'$ has taken place during ECAP.

Figure 1b shows the evolution of the volume fractions of γ, α' and ε phases during ECAP. It can be seen that, with increasing strain, the volume fraction of the γ phase decreases markedly, whereas the α' phase increases significantly. After eight passes, the volume fraction of α' phase has increased to ~83%. For the ε phase, it is hard to determine its volume fraction from XRD, because only the (101) reflection peak is present. Alternatively, we estimated its area fraction in TEM (for each pass, more than four samples and 40 different areas were analysed) and the result is also shown in figure 1b. Here, the fraction of ε phase was not included in the total fraction of phases. In this case, the area fraction of ~8% was estimated roughly after one pass, and decreased with increasing passes. There was no ε phase detected after six passes in TEM, which was consistent with the XRD result. It is reasonable to conclude that ε phase formed at the beginning passes has transformed to α' phase via $\varepsilon \rightarrow \alpha'$ during further straining. The $\varepsilon \rightarrow \alpha'$ phase transformation has been identified in 304 SS during uniaxial tension [36].

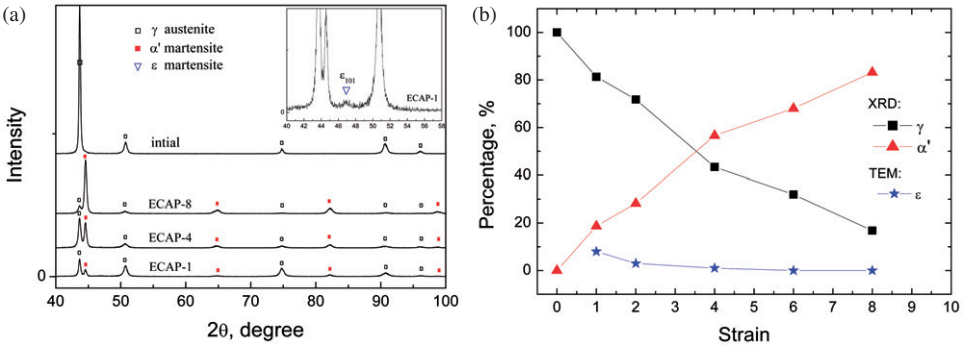

Figure 1. (a) XRD profiles of the initial and post-ECAP samples; (b) volume/area fractions of γ, α' and ε phases vs. strain (passes).

3.2. *Microstructural evolution*

3.2.1. OM observations. The optical microstructure of the initial sample is shown in figure 2a, which is characterized by equiaxed grains with sizes of 200–400 μm with some annealing twins present. After one pass by ECAP, most of the grains were elongated, forming many shear/deformation bands within the elongated grains, as shown in figure 2b. An additional pass generated grains that were more severely elongated and the initial GBs were difficult to identify (figure 2c). After four passes, the microstructure became homogeneous and only deformation traces can be seen along the ECAP shear direction, as shown in figure 2d. Higher strains resulted in the microstructures similar to that produced after four passes.

3.2.2. Formation of nanocrystalline γ austenite. Shear bands are typical microstructural features after the first and second pass. Figure 3a is a bright-field TEM micrograph of the deformation microstructure in the one-pass sample. Several primary shear bands were observed, as indicated by arrows. These primary shear bands subdivided a grain into several small blocks, which consisted of many fine bands. Figure 3b is an enlarged image of figure 3a, showing the detailed microstructure of one primary shear band. A number of submicron and nanometre-sized grains have been formed within the primary shear band,

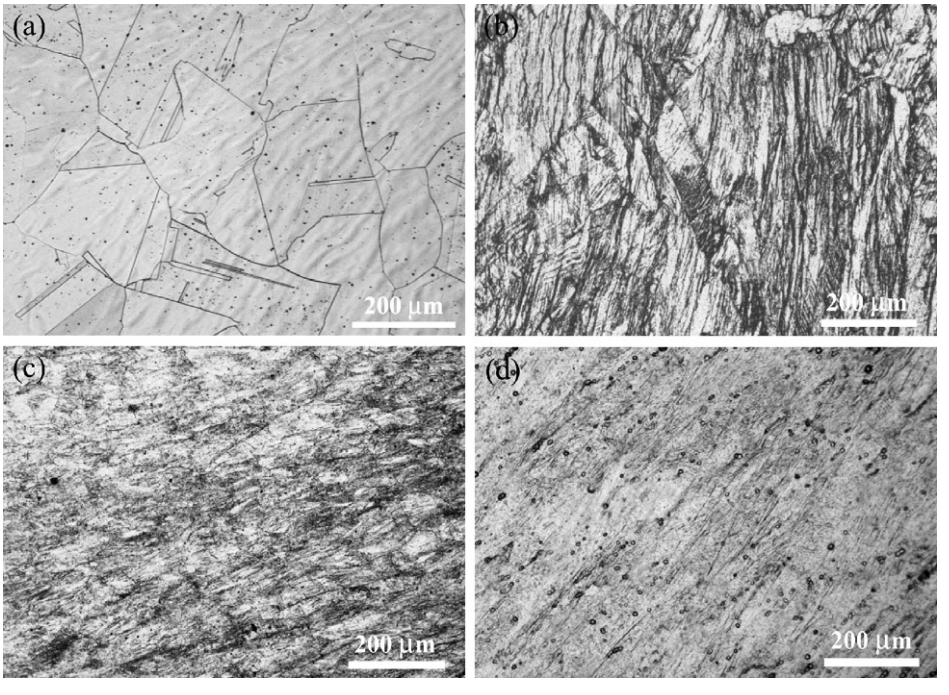

Figure 2. Optical images showing the microstructures of samples: (a) initial; (b) one pass; (c) two passes; (d) four passes.

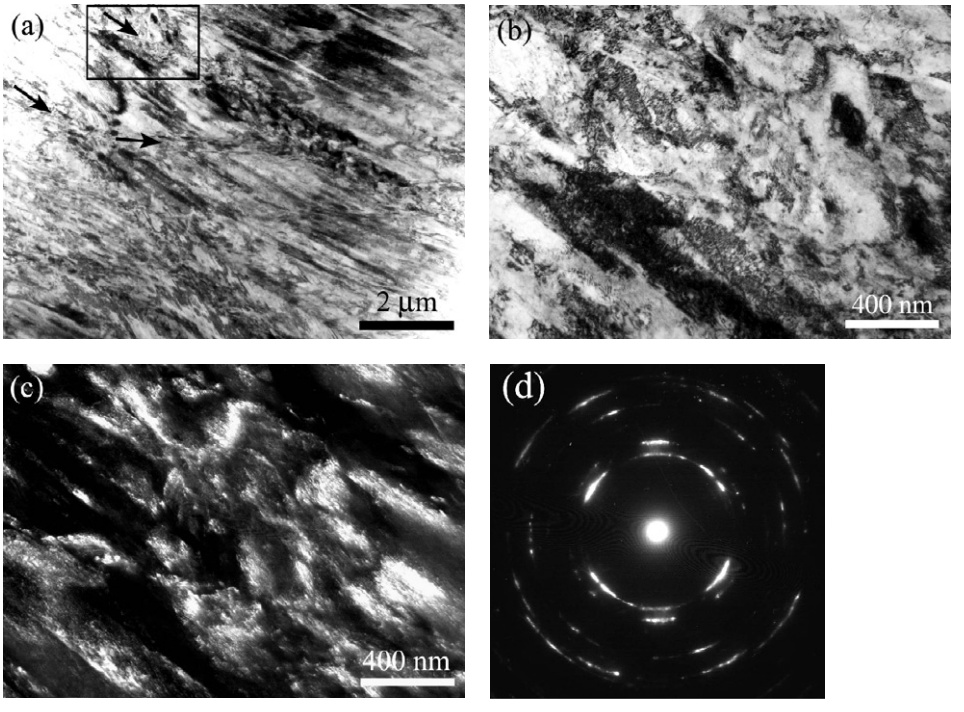

Figure 3. (a) Bright-field TEM micrograph showing shear bands in the one-pass sample; (b) high magnification of the black frame in (a); (c) dark-field image of (b); (d) corresponding SAD pattern of (b).

and they are clearly seen in the dark-field micrograph in figure 3c. The corresponding selected-area diffraction (SAD) pattern (figure 3d) shows discontinuous rings, indicating that many different orientations existed among the fine grains.

In addition to shear bands, deformation twins were widely observed in the parent austenite after deformation. Figure 4a is a typical bright-field TEM micrograph showing the networks of deformation twins on three {111} planes in the one-pass sample. The inset is the corresponding SAD pattern, which consists of two sets of [011] twin diffraction patterns. A high density of deformation twins with widths of several tens of nanometres were formed on the $(11\bar{1})$ plane, whereas the intersections of twins on the other two planes resulted in the formation of submicron-sized rhombic blocks. Figure 4b shows a shear deformation from $\sim 30^{\circ}$ with respect to the twin lamellae in the two-pass sample, which caused a cutting of the twin lamellae. It is expected that the thin twin lamellae will be cut up successively with increasing strain. Figure 4c shows such a microstructure where the twin lamellae lie in fragments forming submicron and nanometer grains, which resulted from the fragmentation of twin lamellae, as indicated by arrows. In the six-pass sample, nanocrystalline grains with a mean grain size of ~ 40 nm can be clearly observed. Figure 4d shows the typical microstructure of austenite in the six-pass sample, which is characterized by many fine fragments of twin lamellae (some of them are outlined with white circles). These fragments formed nanocrystallites. The corresponding

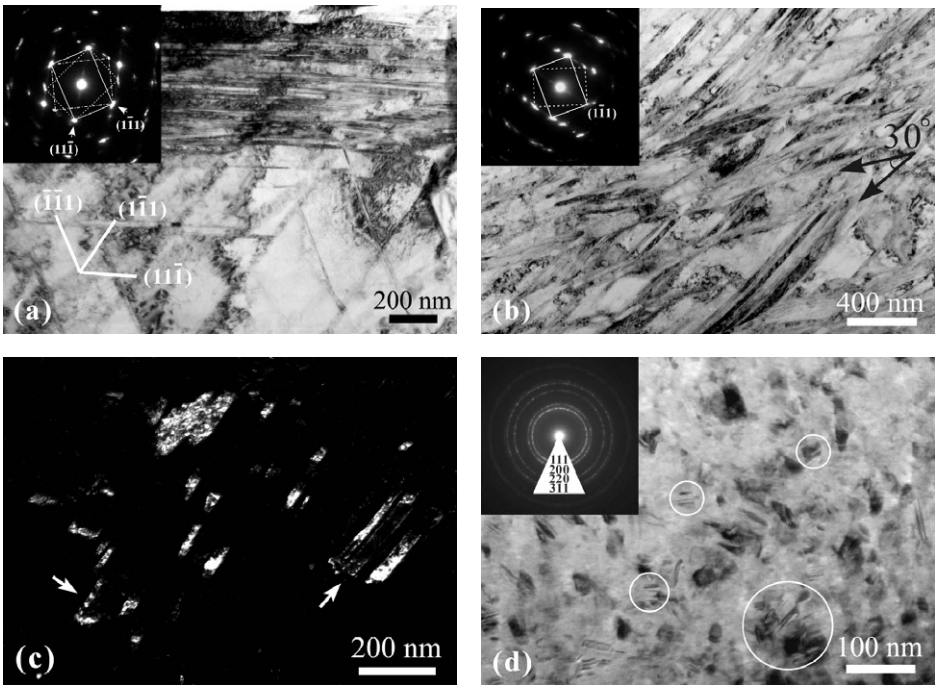

Figure 4. Typical TEM images showing the microstructures of γ austenite ECAPed for (a) one, (b) two, (c) four and (d) six passes. The insets of (a) and (b) are the corresponding SAD patterns with zone axis [011]. The micrograph in (c) is a dark-field image.

SAD pattern (identified as fcc polycrystalline austenitic SS) shows fairly uniform rings, indicating random crystallographic orientations among the nanograins.

The average twin lamella thickness and grain size of γ austenite measured from TEM observations during ECAP are shown in figure 5a. It can be seen that most of the twin lamellae formed during the first and second pass are below 100 nm. This implies that the final grain size resulted from the fragmentation of twin lamellae could be very fine. After six passes, the austenitic grains have been refined to ~40 nm. With further pressing to eight passes, the grain size decreases little and is ~31 nm.

3.2.3. Formation of nanocrystalline α' martensite. At low plastic strain, the nucleation of α' martensite from the parent γ matrix is the first step for the formation of α' nanograins. Figure 6a shows a bright-field TEM micrograph of the one-pass sample, exhibiting a grid-shaped microstructure. It is seen that the grain was subdivided into many small grids with size of ~1 μm by irregular walls. In each grid, a lamellar structure with nanometre-width platelets is visible. Figure 6b is a high magnification image of the outlined region in figure 6a. The corresponding SAD pattern in figure 6d shows composite diffractions of γ matrix, twin and ε martensite with the zone axes $[\bar{1}10]_{\gamma}//[1\bar{1}0]_{\text{twin}}//[11\bar{2}0]_{\varepsilon}$. Figure 6c is a dark-field

image of ε martensite, taken using the $(1\bar{1}01)_{\varepsilon}$ diffraction spot. It can be seen that the ε martensite has been formed from the grid, forming the wall. Consequently, the lamellar microstructure in grids in figure 6a is composed of platelets with alternative stacking of γ matrix, twin and ε martensite, whereas the walls consist of ε martensite.

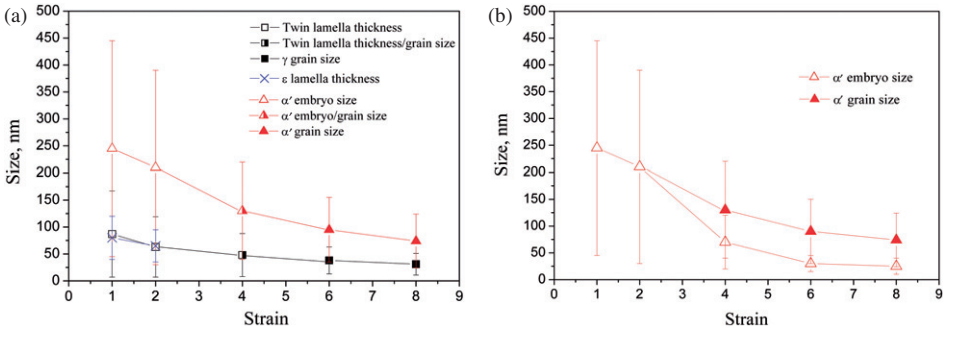

Figure 5. Variation of microstructural sizes with strain (passes). The microstructural sizes include the thickness of twins and ε platelets, γ grain size and α' nuclei/grain size.

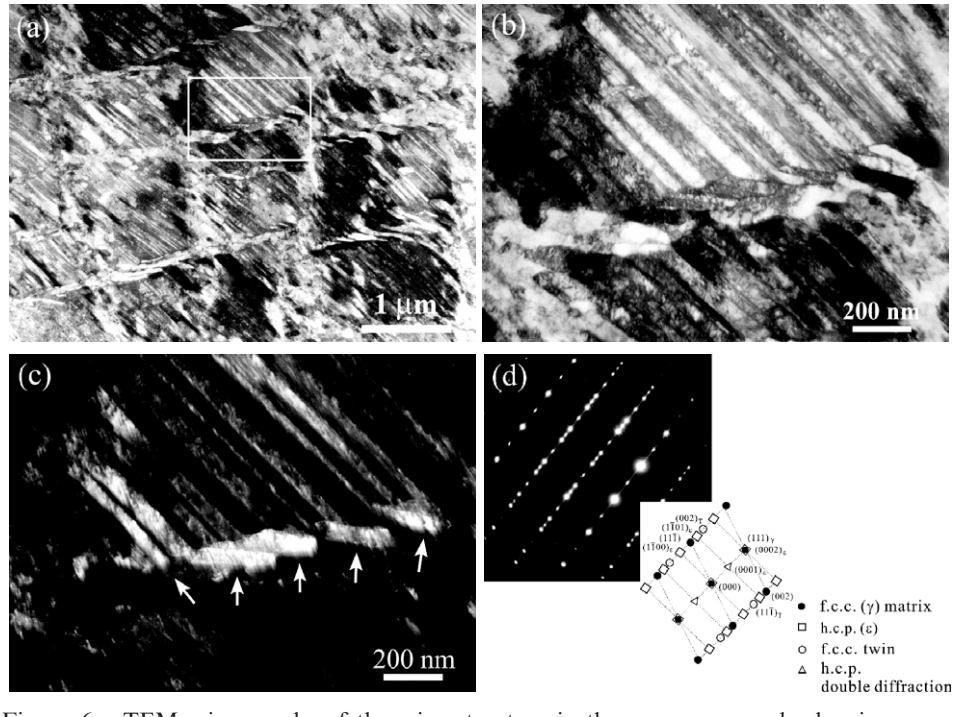

Figure 6. TEM micrographs of the microstructure in the one-pass sample showing $\gamma \rightarrow \varepsilon$ martensite transformation: (a) a grid-shaped microstructure; (b) high magnification of the white frame in (a); (c) dark-field image of ε-martensite (indicated by arrows); (d) corresponding SAD pattern with zone axis $[\bar{1}10]_{\gamma}//[1\bar{1}0]_{\text{twin}}//[11\bar{2}0]_{\varepsilon}$.

The $\gamma \rightarrow \varepsilon$ transformation resulted in largely coherent hcp platelets with the (0001) habit plane strictly complying with the following orientation relationship, namely $(0001)_{\varepsilon}//\{111\}_{\gamma}$ and $<11\bar{2}0>_{\varepsilon}//<110>_{\gamma}$. As indicated by Fujita and Ueda [30], the $\gamma \rightarrow \varepsilon$ transformation is caused by passage of $1/6 < 11\bar{2} >$ Shockley partial dislocations through alternative $\{111\}_{\gamma}$ planes, i.e. overlapping of SFs on every second slip plane resulting in the formation of ε martensite.

The ε phase is only an intermediate phase during the formation of α' martensite, as indicated by the XRD profiles in figure 1. Figure 7 further reveals the $\gamma \rightarrow \varepsilon \rightarrow \alpha'$ transformation clearly in the one-pass sample. As shown in figure 7a, several irregular submicron and nanometre-sized grains are embedded within a lamellar matrix with extensive nanometre-width platelets. According to the SAD pattern taken from the outlined region in figure 7a, the composite diffractions of

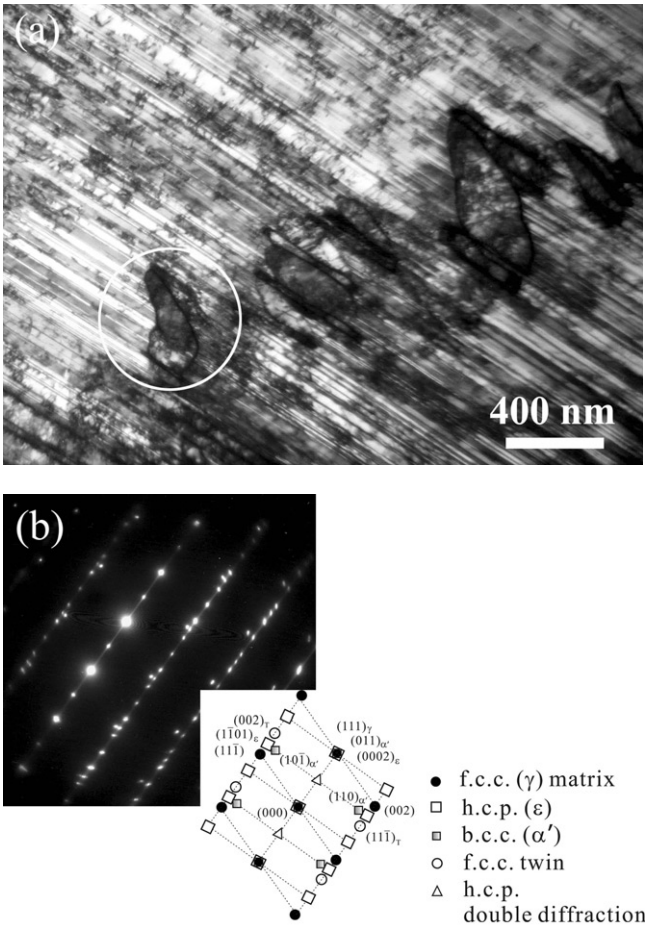

Figure 7. Typical TEM micrographs of the microstructure in the one-pass sample showing $\gamma \rightarrow \varepsilon \rightarrow \alpha'$ martensite transformation in multiple stacked platelets: (a) bright-field image; (b) corresponding SAD pattern with zone axis $[110]_{\gamma}//[1\bar{1}0]_{\text{twin}}//[11\bar{2}0]_{\varepsilon}//[1\bar{1}1]_{\alpha'}$.

γ matrix, twins, ε and α' martensites are identified with the zone axes $[\bar{1}10]_{\gamma}//[1\bar{1}0]_{\text{twin}}//[11\bar{2}0]_{\varepsilon}//[1\bar{1}1]_{\alpha'}$. It is obvious that the lamellar matrix consists of platelets of γ matrix, twin and ε martensite, whereas the irregular grains are the α' martensites. The crystallographic relationships among γ, ε and α' determined from the SAD pattern follow the Kurdjumov–Sachs (K-S) orientation relationship [37, 38], i.e. $\{111\}_{\gamma}//\{0001\}_{\varepsilon}//\{011\}_{\alpha'}$ and $<\bar{1}10>_{\gamma}//<11\bar{2}0>_{\varepsilon}//<1\bar{1}1>_{\alpha'}$.

In addition to the nucleation of α' martensite within the multiple stacked lamellae of twins and ε platelets, there are also α' martensites nucleating at the intersections of micro-shear bands, as indicated by the arrows in figure 8. The micro-shear bands can be deformation twins, stacking faults or ε platelets [31, 36, 38, 39].

With increasing strain, the growth of α' martensite took place via repeated nucleation of α' nuclei and their coalescence with each other. Figure 9a shows a case where two α' bands (indicated by arrows) were formed via the coalescence of many α' nuclei in the two-pass sample. Figure 9b shows the enlarged image of the outlined region in figure 9a. It is seen that several nano-sized α' nuclei have formed together, still having the K-S orientation relationship with the γ matrix (zone axes $[\bar{1}10]_{\gamma}//[1\bar{1}0]_{\text{twin}}//[11\bar{2}0]_{\varepsilon}//[1\bar{1}1]_{\alpha'}$). The similar contrast of the nuclei suggests that only small misorientations exist among them. These nuclei can also be regarded as dislocation cells/subgrains, which may form individual nanocrystallites upon further straining.

Strain-induced dislocation activities were also frequently observed in large-sized α' grains. Figure 10 shows a typical bright-field TEM micrograph that confirms that submicron and nanometre-sized subgrains were produced through various dislocation activities in the two-pass sample. The incident electron beam was parallel to the zone axis of $[\bar{1}11]_{\alpha'}$. Low-angle GBs were found between grains 1 and 2, and grains 2 and 3, as indicated by the white arrows. In grain 1, a number of dislocations

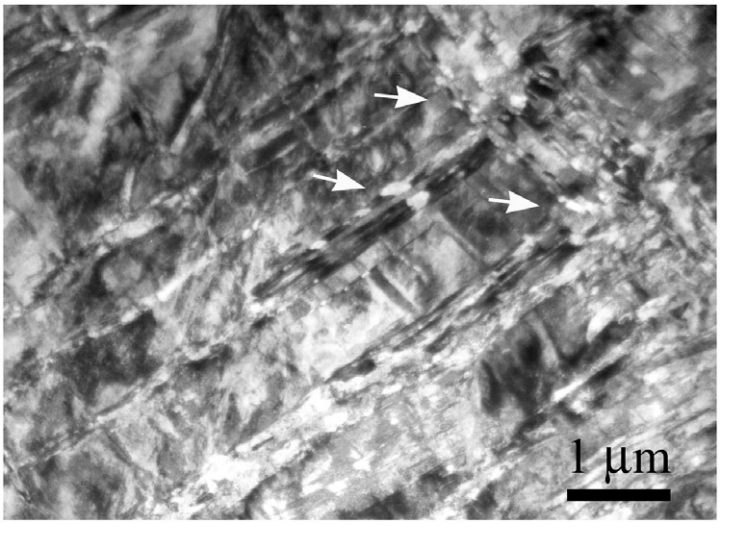

Figure 8. Nucleation of α' martensites (indicated by white arrows) at the intersection of micro-shear bands.

on the $(01\bar{1})_{\alpha'}$ plane glided towards the low-angle GB. With successive accumulation of glissile dislocations, the low-angle GBs finally evolved into high-angle GBs, such as the sharp GB, as indicated by the black arrowheads. In grain 3, dislocation tangles were observed, forming dislocation cells with sizes of several tens of nanometres. These dislocation cells may form individual nano-sized subgrains/grains with further straining, such as grain 4.

At intermediate plastic strain, the coalescence and dislocation-subdivision of α' grains competed with each other upon plastic straining, producing large amounts of α' martensite with a small grain size. Figure 11a shows a typical TEM micrograph of the microstructures obtained in the four-pass sample. It can be seen that typically equiaxed α' grains with sizes of several hundred nanometres have been formed.

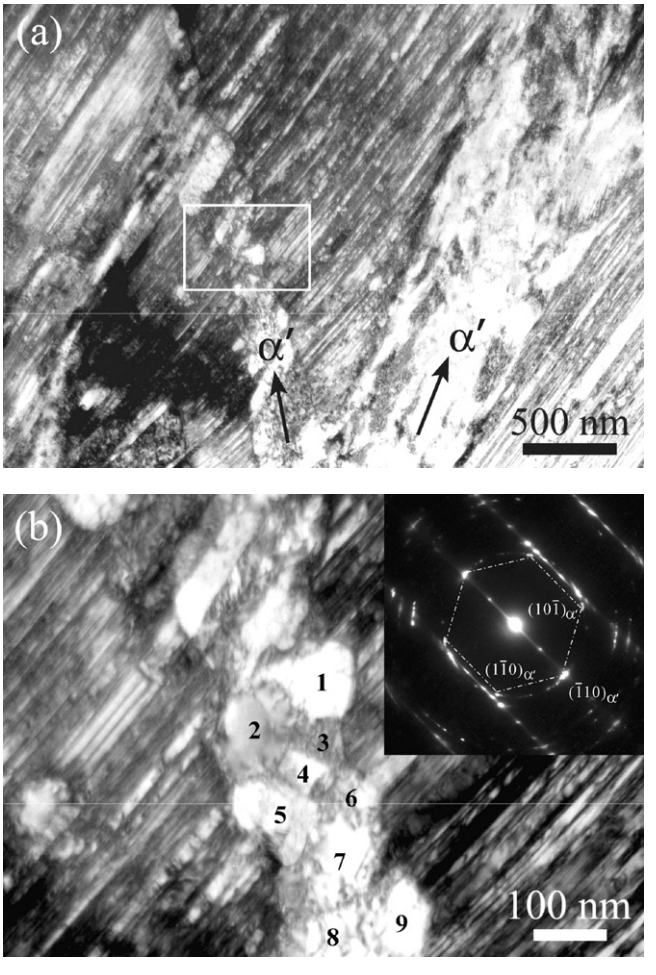

Figure 9. (a) Typical TEM micrographs of the microstructures in the two-pass sample showing the coalescence of α' martensites; (b) high magnification of the white frame in (a). The inset in (b) is the corresponding SAD pattern with zone axis $[\bar{1}\bar{1}0]_{\gamma}//[1\bar{1}0]_{\text{twin}}//[11\bar{2}0]_{\varepsilon}//[1\bar{1}\bar{1}]_{\alpha'}$.

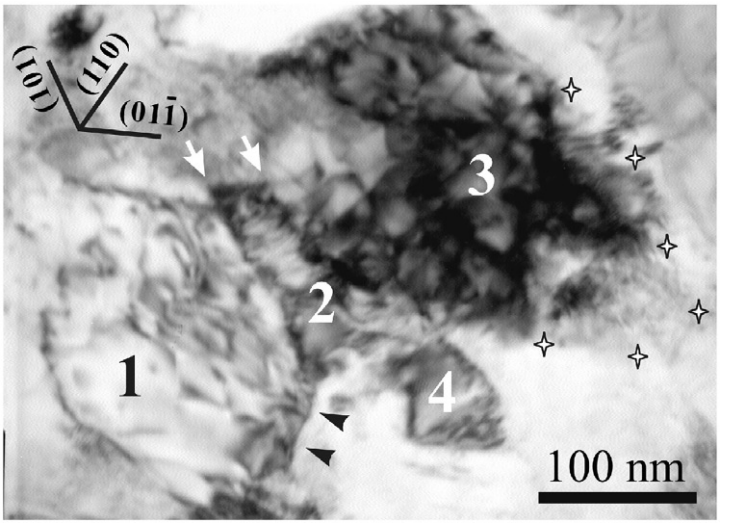

Figure 10. Typical TEM micrograph showing the dislocation microstructures in α' martensite in the two-pass sample. The incident beam is parallel to zone axis $[\bar{1}11]_{\alpha'}$.

Most grains were heavily strained and contained high density of dislocations. The contrasts in many grains are inhomogeneous but varied from place to place, indicating the formation of finer subgrains in the interior, as indicated by the arrows in figure 11a. The corresponding SAD pattern (identified as bcc polycrystalline α' martensite) shows a set of rings, indicating the existence of highly misoriented grains. Figure 11b shows another morphology of α' martensite formed in the four-pass sample, which is characterized by a lamellar structure with a dimension of several tens of nanometres in width and a few hundred nanometres in length. In the corresponding SAD pattern, discontinuous rings were formed through the diffusion of (110) diffraction spots (zone axis $[\bar{1}11]_{\alpha'}$), implying that the α' bands might be transformed from the matrix stacked by γ, twins and/or ε platelets (likely to be the matrix in figure 7a). Different contrasts appeared in the lamellar interiors, indicating that they will be cut into nanograins by dislocations similar to the case in twin lamellae (see figure 4).

After four passes, the γ austenite has been refined to submicron level. The DIMT taking place from the submicron-sized γ grains produced a lot of nanometre-sized α' grains. Figure 12a shows the mixtures of γ and α' grains in the four-pass sample. It is seen that many α' grains nucleated at the GB of a twinning grain, γ_1. The crystallographic relationship between α'_1 and γ_1 still obeys the K-S relationship, as identified by the corresponding SAD pattern (zone axes $[011]_{\gamma}//[0\bar{1}\bar{1}]_{\text{twin}}//[111]_{\alpha'}$) in figure 12b, pattern A. The different contrasts among the α' grains indicate that though they were in contact with each other, they did not coalesce to form larger α' grains, i.e. they are individual nanocrystallites. For instance, the SAD pattern in figure 12b, pattern B, taken from the region enclosing grains γ_1, α'_1 and α'_2, indicates that a misorientation angle of $\sim 9^\circ$ has been developed between grains α'_1 and α'_2. This large misorientation angle can prevent their coalescence.

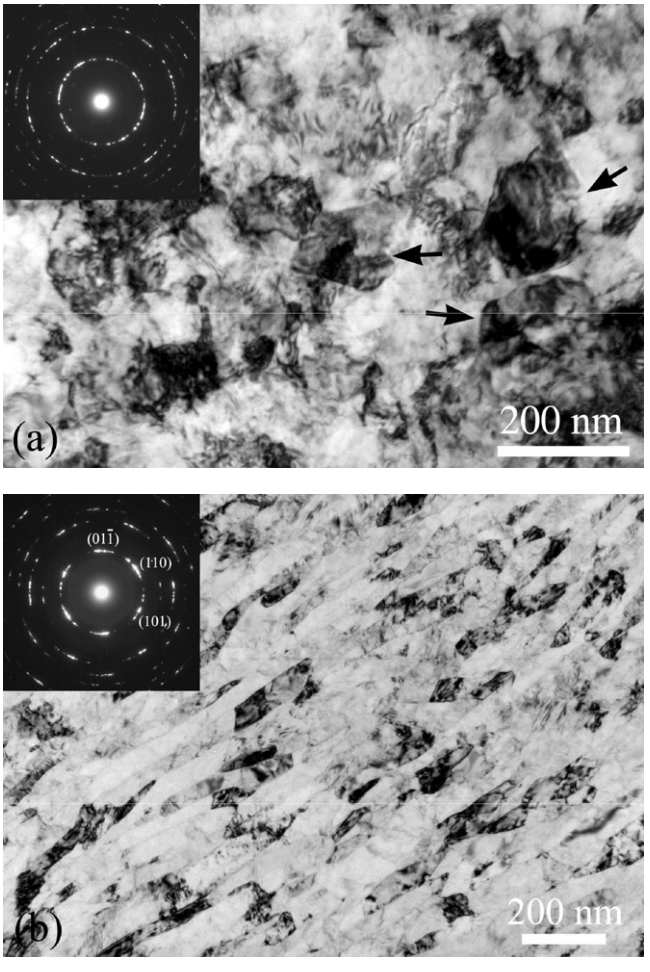

Figure 11. Typical TEM micrographs showing the equiaxed (a) and elongated (b) grain structures of α' martensite in the four-pass sample. The insets are the corresponding SAD patterns close to zone axis $[\bar{1}11]_{\alpha'}$.

Apparently, grain α'_2 has rotated with respect to α'_1, resulting in the deviation of K-S orientation relationship between α'_2 and γ_1. Figure 12b shows the dark-field image of three α' grains by using $(10\bar{1})_{\alpha'}$ diffraction spots. It can be seen that dislocation activities are still in progress in these nanocrystallites.

At high plastic strain, figure 13a shows the typical microstructure of α' martensite in the six-pass sample. Nanograins with an average grain size of ~90 nm have been achieved. Close examinations show that grain subdivision via dislocation activities still took place in grains with relatively large size. In figure 13b, the bright- and dark-field images reveal the detailed microstructure of a grain (indicated by the arrow in figure 13a) with a size of ~160 nm, when the [111] zone axis of the grain was tilted parallel to the incident electron beam. A dislocation pile-up near GB is visible, forming a subgrain boundary, as indicated by the arrow-heads. The boundaries

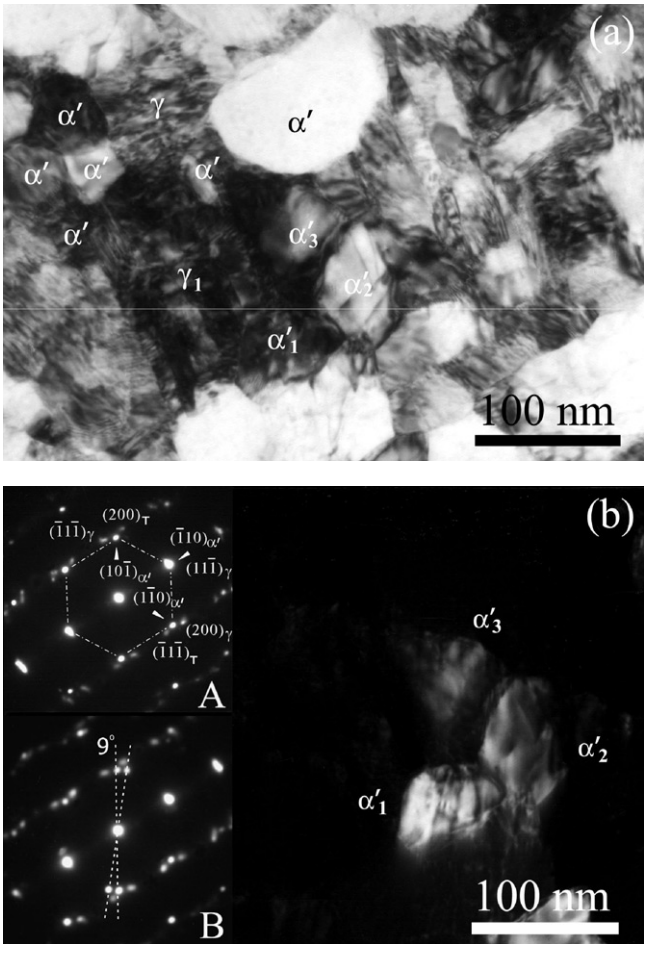

Figure 12. Typical TEM micrographs showing $\gamma \rightarrow \alpha'$ martensite transformation in submicron-sized austenite: (a) bright-field image and (b) dark-field image. The corresponding SAD pattern A in (b) with zone axis $[011]_{\gamma}//[0\bar{1}\bar{1}]_{\text{twin}}//[111]_{\alpha'}$ encloses grains γ_1 and α'_1, whereas pattern B encloses grains γ_1, α'_1 and α'_2.

divided the parent grain into three nanometre-sized subgrains with dislocation-free interiors.

Figure 14a is a typical bright-field TEM micrograph that shows the microstructure of α' martensite in a large area in the eight-pass sample, with an average grain size of ~74 nm. The microstructure is characterized by both equiaxed and elongated nanograins, as shown clearly in the dark-field image (figure 14b). The corresponding SAD pattern (taken from an area with a diameter of 1 μm) was identified as bcc polycrystalline α' martensite and consisted of a set of uniform rings, indicating high misorientations among these α' nanograins.

Figure 15a shows an interesting finding, i.e. that fairly tiny nanograins with sizes ranging from several nanometres to ~30 nm were produced in the eight-pass sample. The corresponding SAD pattern in figure 15c reveals both γ phase and α' martensite.

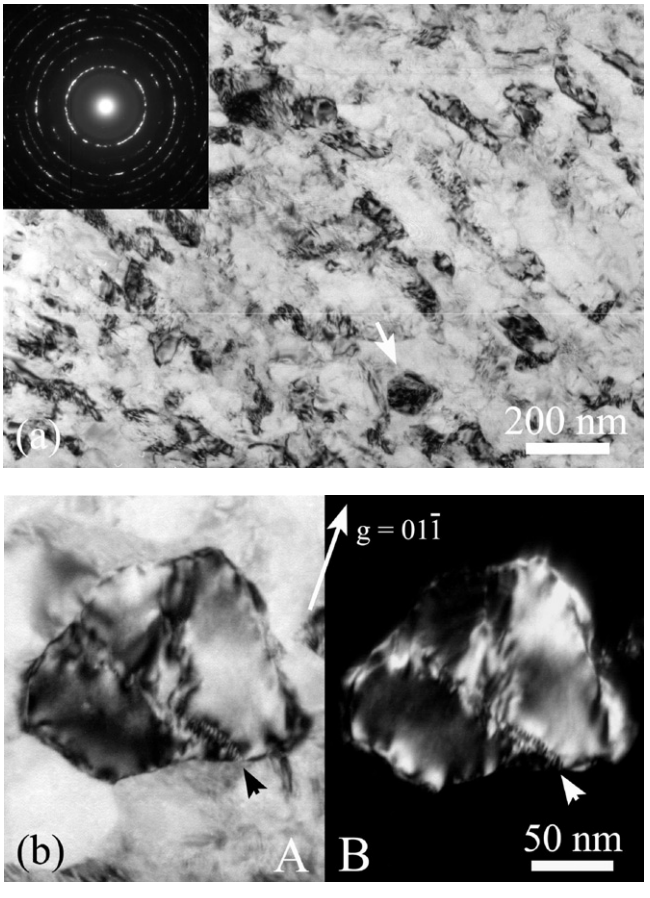

Figure 13. (a) Typical TEM micrograph together with corresponding SAD pattern showing the microstructures of α' martensite in the six-pass sample; (b) bright-field (A) and dark-field (B) TEM micrographs showing the detailed microstructure of a ~160 nm grain indicated by the white arrow in (a).

Figure 15b is the dark-field image of nanocrystalline α' martensite obtained from a portion of the $\{200\}_{\alpha'}$ ring, as illustrated by the white circle in figure 15c. The α' nanocrystallites with diameters ranging from several nanometres to ~15 nm can be clearly seen. It has been shown that nanocrystalline γ grains with an average grain size of ~30 nm have been produced after eight passes. Hence, finer α' nanocrystallites should be formed via DIMT at manometer scale, i.e. transformed from the γ nanocrystallites.

The average nucleus/grain sizes of α' martensite as a function of strain measured from TEM are summarized in figure 5a. As shown, the nucleus size at low plastic strains could range from several tens of nanometres to more than 400 nm. Though there are coalescences of α' nuclei hindering grain refinement, the average size of α' grains can still be decreased to ~130 nm at a strain of 4. At high plastic strain of 6 and 8, nanocrystalline α' martensite with average grain sizes of ~90 nm and ~74 nm, respectively, were finally achieved. The successive decrease in grain size of α'

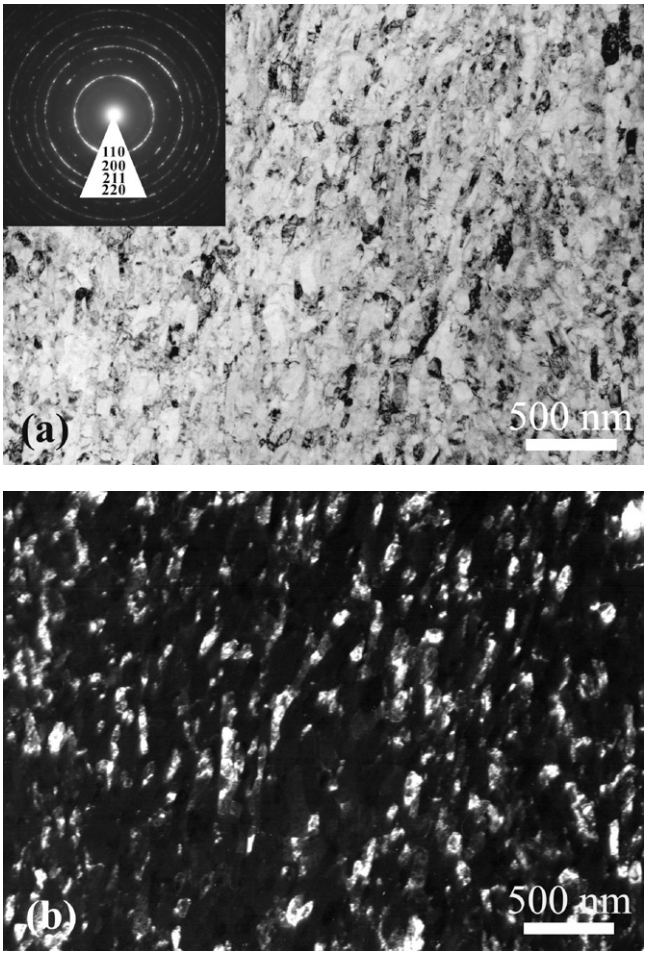

Figure 14. TEM micrographs of nanocrystalline α' grains in the eight-pass sample: (a) bright-field image with corresponding SAD pattern inset and (b) dark-field image.

martensite at intermediate and high plastic strains should be attributed to two different refinement mechanisms, i.e. dislocation subdivision of large grains and martensite transformation taking place in submicron and nanometre γ grains (see figure 5b), which produced a lot of nanocrystallites.

4. Discussion

Microstructural investigations revealed that two kinds of nanostructures were achieved in ultra-low carbon SS after ECAP deformation for eight passes: (a) nanocrystalline γ austenite with an average grain size of $\sim$31 nm and (b) strain-induced nanocrystalline α' martensite with a size of $\sim$74 nm. Based on the TEM observations, different formation mechanisms in γ and α' phases have

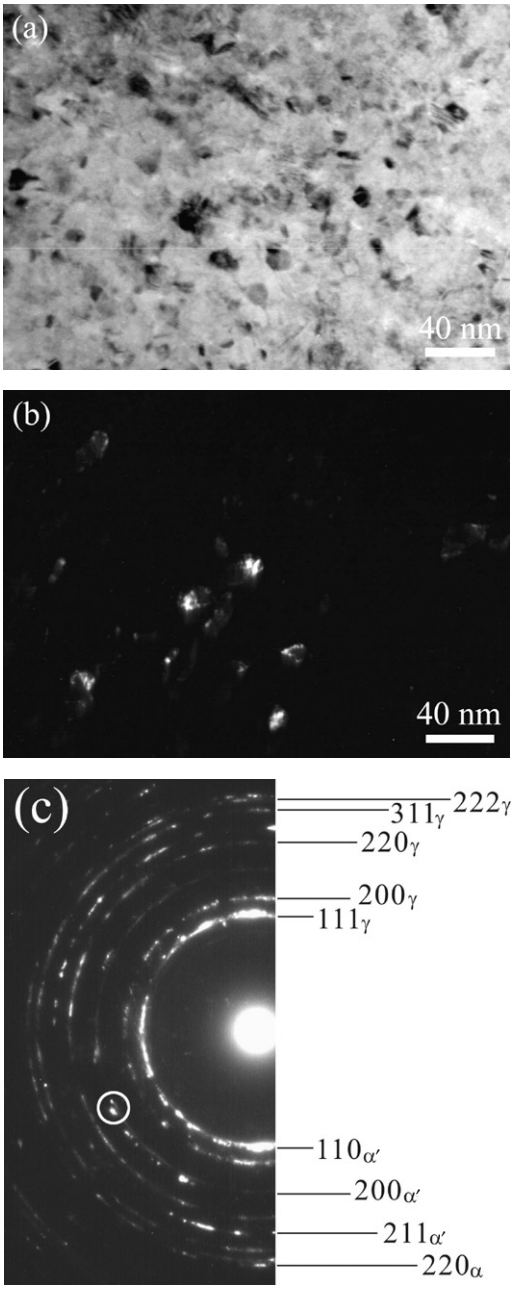

Figure 15. (a) Bright-field TEM micrograph showing very fine nanocrystalline grains; (b) dark-field TEM micrograph of α' nanocrystallites taken from a portion of the $\{200\}\alpha'$ ring, as illustrated by the white circle in (c); (c) corresponding SAD pattern of (a).

been detected. In the following sections, the formation mechanisms will be discussed in terms of strain accommodation in γ and α' phases at different strain levels.

4.1. *Formation mechanism of nanocrystalline γ austenite*

Deformation twinning is an important deformation mechanism in SS, especially at large plastic strains. At the beginning of the ECAP process, severe plastic shear strain produced a high density of deformation twins with thicknesses of several tens of nanometres. These twin boundaries subdivided the original grains into thin twin-matrix lamellae and/or submicron-sized rhombic blocks. With subsequent pressing, the twin-matrix lamellae were successively cut up due to the shear deformation from different directions, because the sample was rotated for 90° in the next pass (figures 4b–c). Tao *et al.* [25] and Wang *et al.* [40] have shown the micro-mechanism of twin fragmentation during the formation of nanostructures in the top surface layers of Inconel 600 alloy and Cu samples subjected to SMAT. Their observations demonstrated that a lot of dislocations and/or dislocation walls rather than micro-twins were introduced into the thin twin–matrix lamellae in order to accommodate plastic deformation. These dislocation walls were eventually developed into GBs, cutting the two-dimensional twin–matrix lamellae into three-dimensional equiaxed nanograins. In the present case of ECAP, real nanocrystalline γ austenite can also be achieved via the twin fragmentation mechanism.

The critical element of twin fragmentation mechanism is the formation of high density of thin twin–matrix lamellae. It is well known that both a high strain rate and a very low temperature are favourable for deformation twinning. However, these deformation conditions are difficult to achieve under ECAP [4, 19]. A low SFE is also beneficial to twinning. For fcc metallic materials, the predominant deformation mechanisms at high plastic strain change gradually from dislocation slip to deformation twinning with decreasing SFE [41, 42]. Accordingly, the grain refinement mechanisms are also transformed from the dislocation-subdivision mechanism to the twin fragmentation mechanism. Then, the levels of the limiting grain sizes resulting from these two refinement mechanisms are also expected to change. Figure 16 presents the limiting grain sizes obtained from ECAP in several typical fcc materials with different SFEs. It is shown that with decreasing SFEs the limiting grain sizes decrease. The minimum grain size achieved in materials with relatively high SFE ($>40\,\mathrm{mJ\,m^{-2}}$) is beyond 150 nm, such as ~200 nm for Cu [10, 19]. This could be attributed to the fast dynamic recovery of dislocations that prevents dislocation boundaries from accumulating on finer scales [10, 19]. In other words, the dislocation cells induced by plastic strain determine the final grain size. However, a low SFE can suppress the rate of dislocation recovery [32]. Furthermore, the twin boundaries are also strong obstacles to dislocation recovery once deformation twinning occurs [42]. A high density of twin lamellae nanometres in width determines that the final grain size could be very fine via subsequent twin fragmentation. For example, a minimum grain size of ~10 nm can be achieved in the surface layer of Cu sample under SMAT, which resulted from the fragmentation of thin twin lamellae [40]. The present findings of nanocrystalline austenitic SS also provide

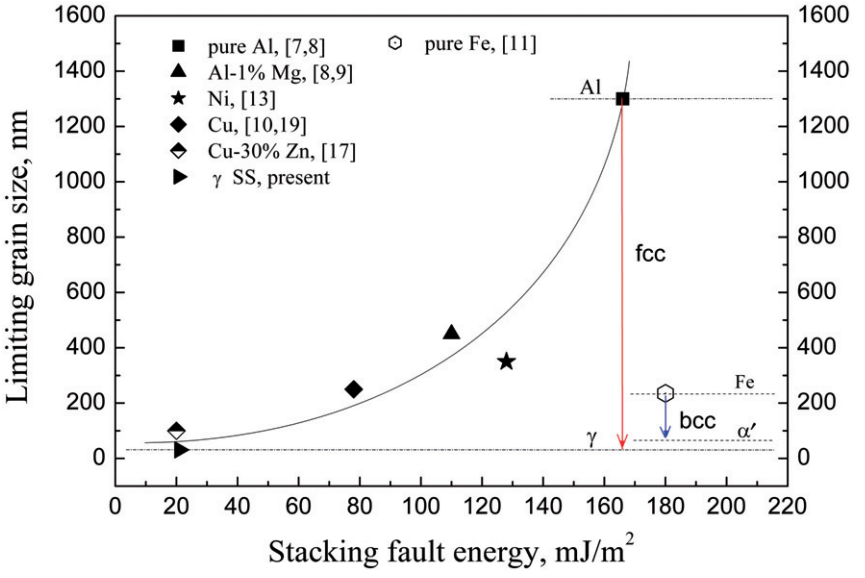

Figure 16. The limiting grain sizes of fcc materials obtained under ECAP vs. SFE [22, 43]. All the grain size data were measured by TEM.

strong evidence to suggest that nanograins could be obtained via the twin fragmentation mechanism in low SFEs fcc materials under ECAP.

In bcc materials, such as pure Fe (180 mJ m^{-2} [43], ~235 nm) [11] and low-carbon steel (~200 nm) [12], it seems that the effect of SFE on the limiting grain size is not as strong as that in fcc materials, as shown in figure 16. It should be noted that the grain sizes obtained in the present SS were a result of various phase transformations (including deformation twinning), whereas those shown in figure 16 were generated by the processes of grain subdivision via the accumulation and rearrangement of dislocations.

4.2. *Formation mechanism of nanocrystalline α′ martensite*

4.2.1. DIMT under ECAP. Austenitic SS is susceptible to martensite transformation under plastic deformation at low temperature, which can be regarded as an additional deformation mechanism to accommodate plastic strain in addition to dislocation slip and deformation twinning. In comparison with conventional deformation processes, the effect of ECAP on DIMT is obvious. For example, by using XRD, Shin *et al.* [44] recently measured the amount of the transformed martensite in 304 SS deformed by ECAP, uniaxial tension and compression, and found that shear deformation achieved by ECAP is the most effective route to trigger martensite transformation. In terms of the present work, one can consider two factors contributing this effect: (a) a large amount of defects produced under ECAP, such as SFs, twins, ε platelets and GBs (figures 4, 6, 7, 12 and 15), which provide many potential nucleation sites for DIMT; (b) the high shear stress (according to the

von Mises criterion, $\tau \approx HV/3\sqrt{3} \approx$700–900 MPa, the Vickers hardness (HV) measured in this paper is 3.7–4.9 GPa of the post-ECAP samples after one to eight passes), which gives a high driving force for DIMT.

The present observations about the microstructures of DIMT under ECAP show several prominent characteristics, especially with decreasing the grain size of γ phase.

(i) In micron-sized γ grains, the α' martensite can nucleate both at the intersections of micro-shear bands (figure 8) and within the multiple stacked platelets of γ, twins and ε (figure 7). In submicron-sized γ grains, the α' martensite prefers to nucleate at the GB of the γ grain (figure 12).

(ii) The nucleation of α' martensite from both micron-sized γ grains (figure 7) and submicron-sized γ grains (figures 12a and 12b, pattern A) obeys the K-S orientation relationship. With increasing shear strain, the K-S orientation relationship was disturbed.

(iii) DIMT can occur in γ nanocrystallites (figure 15). However, due to the limitation of TEM resolution, it is difficult to identify the nucleation site and the orientation relationship between α' and γ nanocrystallites in the present work. In 304 SS, the critical size for the nucleation of α' martensite is about 5–7 nm, as evidenced by Staudhammer *et al*. [31], which is also consistent with the present observations (figures 7, 8, 12 and 15). The finding of DIMT in nanocrystalline γ grains suggests that a new deformation mechanism in addition to dislocation slip and deformation twinning is active in nanocrystalline austenitic steel.

Traditionally, the $\gamma \rightarrow \alpha'$ transformation occurs via two shear strains of specific defects (mostly characterized by the type of $a/6 < 11\bar{2} >$ Shockley partial dislocation) on the $\{111\}_\gamma$ planes [29, 31]. Depending on the crystallographic directions of the second shear deformation, the K-S or the Nishiyama–Wessermann orientation relationship could result. In the K-S relationship, the $\{111\}_\gamma$ is converted into the $\{110\}_{\alpha'}$ with the $< \bar{1}10 >_\gamma$ parallel to the $< \bar{1}11 >_{\alpha'}$ [37, 38]. This mechanism could be reasonable for DIMT in large-sized γ grains. However, it is unclear whether the K-S relationship still applies in nanocrystalline γ austenite or not. As is well known, plastic deformation mechanisms are strongly affected by grain size. For example, GB sliding and grain rotation are active when the grain size is decreased to ~10 nm [45]. Besides, the mechanisms of deformation twinning are also transformed from the pole mechanism in coarse grains to partial dislocation emission from GBs, when the grain size is decreased to several hundred of nanometres [19]. Hence, there is a possibility that the DIMT mechanism could change with a decrease of the size of γ grains to the nanoscale. Recently, a reverse shear-induced $\alpha \rightarrow \gamma$ transformation with the K-S orientation relationship was found in nanocrystalline Fe–C composite, and the authors argued that the atomistic mechanism was likely to proceed by glide of the ordered arrays of transformation partials $1/6 < 1\bar{1}0 >_{bcc}$ on every $\{111\}_{fcc}$ plane [46]. It is uncertain whether a similar mechanism is suitable for the $\gamma \rightarrow \alpha'$ transformation in nanocrystalline austenitic SS or not.

4.2.2. Formation of nanocrystalline α' martensite from DIMT. A large amount of microstructural observations (figures 6–14) show that the predominant refinement

process during the formation of nanocrystalline α' martensite is the successive DIMT ($\gamma \rightarrow \varepsilon \rightarrow \alpha'$ and $\gamma \rightarrow \alpha'$) from γ grains with sizes ranging from microns to nanometres. In order to accommodate plastic deformation of α' itself, the coalescence of α' nuclei and dislocation activities in large-sized α' grains are also operative.

At low plastic strain, accompanied by the formation of deformation twins, the $\gamma \rightarrow \varepsilon$ transformation produced a high density of ε platelets with thicknesses of only several tens of nanometres (figures 6–7). These thin ε platelets induced a refinement effect similar to that of twin lamellae, which subdivided the grains into lamellar structures. The contribution of $\gamma \rightarrow \varepsilon$ transformation to grain refinement has been identified in Co deformed by SMAT [47]. The formation of ε martensitic walls observed in our samples (figure 6) also acted as ''GBs'', subdividing the original large grains into small blocks. Following the formation of deformation twins and ε platelets, α' martensite nucleated at the stacked layers of γ, twin and ε platelets. Without the assistance of ε phase, α' martensite can nucleate at the intersections of micro-shear bands including γ and twin platelets (figure 8), which are also favourable nucleation sites [31, 36]. In both cases, the size of α' nuclei, which can be regarded as α' grains, is of several tens/hundreds of nanometres (figure 5). The amount of α' grains induced at low plastic strain (<4) is $\sim$40% (figure 1b), i.e. a half of the α' phase in total ($\sim$83%).

At intermediate to high plastic strains, another half amount of α' phase was produced. The average sizes of this part of α' nuclei transformed from the submicron and nanometre-sized γ grains are of only $\sim$68 nm and $\sim$24 nm at intermediate and high plastic strains, respectively, as shown in figure 5b. It should be pointed out that the nanocrystalline α' nuclei do not tend to coalesce together, but are prone to evolve into individual nanocrystallites (figures 12 and 15), which is important for the formation of nanocrystalline α' martensite. It is the DIMT in small-sized γ grains that produces nanocrystalline α' martensite.

One factor that opposes the formation of nanocrystalline α' martensite is the coalescence of α' nuclei due to minimizing the bulk free energy. In order to coalesce, the nuclei must be misoriented by a small angle [31, 48]. According to the K-S orientation relationship, a partially coherent interface forms between α' nucleus and its parent γ grain [49]. Thus, once two nuclei come into contact within the same parent austenitic grain, they will merge to a large one. The coalescence of α' nuclei is prevalent at low plastic strain, because the α' can nucleate within the same parent γ grain and keep the K-S orientation relationship (figures 7 and 9). However, such coalescence becomes unnecessary when the parent γ grain size is decreased to submicron and nanometre scale. The numbers and the orientations of α' nuclei are dependent on the parent γ grains. From TEM observations, a submicron-sized γ grain can be transformed into several nanometre-sized α' martensites from GBs (figure 12), whereas a nanometre-sized γ crystallite probably could only be transformed into one α' martensite (figure 15). Besides, the orientation of a new α' is determined by its parent γ grain. Therefore, the part of nanocrystalline α' martensite transformed from the highly misoriented nanocrystalline γ grains could also be randomly orientated.

Although α' nuclei coalesce together, dislocation walls still subdivide the nuclei, which are involved in the refinement mechanism via dislocation slip.

The multiplication of dislocations and their evolution to dislocation walls and further to GBs are active in large-sized α' grains, which is similar to those occurring in *fcc* metals with relatively high SFEs [7, 8]. This dislocation process proceeds at all strain levels (figures 9–13). Apparently, an effect of grain refinement is achieved from this dislocation-subdivision mechanism.

5. Conclusions

Bulk nanocrystalline grain microstructures were successfully achieved in an ultra-low carbon SS by means of ECAP at RT. Two types of nanocrystalline grains were formed: (i) nanocrystalline γ austenite with an average grain size of $\sim$31 nm, and (ii) strain-induced nanocrystalline α' martensite with a size of $\sim$74 nm. From microstructural examinations, different formation mechanisms were identified during the creation of nanocrystalline γ austenite and nanocrystalline α' martensite.

For γ austenite, the grain refinement is primarily achieved via deformation twinning and subsequent twin fragmentation. It is suggested that for fcc materials, a very low SFE is especially favourable for the formation of nanocrystalline grains by ECAP at RT.

For α' martensite, the successive DIMT ($\gamma \rightarrow \varepsilon \rightarrow \alpha'$ and $\gamma \rightarrow \alpha'$) from γ austenite produces numerous α' nuclei with size ranging from several tens of nanometres to several hundreds of nanometres. The nuclei could coalesce to form large-sized α' grains. However, it is complemented by the dislocation-subdivision mechanism upon plastic deformation. It is found that the highly misoriented γ grains with submicron and nanometre sizes are of great advantage for the formation of nanocrystalline α' via DIMT.

DIMT can take place in submicron-sized γ grains. The α' martensite nucleates at the GBs of a γ grain and obeys the K-S orientation relationship. DIMT occurs in nanocrystalline γ grains and may represent a new deformation mechanism for the plastic deformation of nanocrystalline austenitic grains.

Acknowledgements

This research was financially supported by the National Natural Sciences Foundation of China (NSFC) under grant Nos. 50701047, 50371090 and 50471082. Zhang ZF would like to thank the financial support of ''Hundred of Talents Project'' by the Chinese Academy of Sciences, and the National Outstanding Young Scientist Foundation under grant No. 50625103.

References

[1] R.Z. Valiev, I.V. Alexandrov, Y.T. Zhu, *et al.*, J. Mater. Res. **17** 5 (2002).
[2] Y.M. Wang and E. Ma, Appl. Phys. Lett. **83** 3165 (2003).
[3] K.M. Youssef, R.O. Scattergood, K.L. Murty, *et al.*, Appl. Phys. Lett. **87** 091904 (2005).

[4] R.Z. Valiev, R.K. Islamgaliev and I.V. Alexandrov, Prog. Mater. Sci. **45** 103 (2000).
[5] K. Lu and J. Lu, Mater. Sci. Engng A **375** 38 (2004).
[6] Y. Saito, H. Utsunomiya, N. Tsuji, *et al*., Acta Mater. **47** 579 (1999).
[7] Y. Iwahashi, Z. Horita, M. Nemoto, *et al*., Acta Mater **46** 3317 (1998).
[8] Y. Iwahashi, Z. Horita, M. Nemoto, *et al*., Metall. Mater. Trans. A **292** 503 (1998).
[9] H. Hasegawa, S. Komura, A. Utsunomiya, *et al*., Mater. Sci. Engng. A **265** 188 (1999).
[10] S. Komura, Z. Horita, M. Nemoto, *et al*., J. Mater. Res. **14** 4044 (1999).
[11] B.Q. Han, E.J. Lavernia and F.A. Mohamed, Metall. Mater. Trans. A **34** 71 (2003).
[12] Y. Fukuda, K. Oh-ishi, Z. Horita, *et al*., Acta Mater. **50** 1359 (2002).
[13] A.P. Zhilyaev, B.K. Kim, J.A. Szpunar, *et al*., Mater. Sci. Engng A **391** 377 (2005).
[14] D.H. Shin, I. Kim, J. Kim, *et al*., Acta Mater. **51** 983 (2003).
[15] I.P. Semenova, G.I. Raab, L.R. Saitova, *et al*., Mater. Sci. Engng A **387** 805 (2004).
[16] T. Liu, Y.D. Wang, S.D. Wu, *et al*., Scripta Mater. **51** 1057 (2004).
[17] K. Neishi, Z. Horita and T.G. Longdon, Mater. Sci. Engng A **352** 129 (2003).
[18] D.A. Hughes and N. Hansen, Acta Mater. **45** 3871 (1997).
[19] C.X. Huang, K. Wang, S.D. Wu, *et al*., Acta Mater. **54** 655 (2006).
[20] D.H. Shin, I. Kim, J. Kim, *et al*., Acta Mater. **51** 983 (2003).
[21] W.S. Choi, H.S. Ryoo, S.K. Hwang, *et al*., Metall. Mater. Trans. A **33** 973 (2002).
[22] L.E. Murr, *in Interfacial Phenomena in Metals and Alloys* (Techbooks, Herndan, VA, 1975).
[23] S. Suwas, L.S. Tóth, J.J. Fundenberger, *et al*., Scripta Mater. **49** 1203 (2003).
[24] I.J. Beyerlein, L.S. Tóth, C.N. Tomé, *et al*., Phil. Mag. **87** 885 (2007).
[25] N.R. Tao, X.L. Wu, M.L. Sui, *et al*., J. Mater. Res. **19** 1623 (2004).
[26] H.W. Zhang, Z.K. Hei, G. Liu, *et al*., Acta Mater. **51** 1871 (2003).
[27] Y.H. Zhao, X.Z. Liao, Y.T. Zhu, *et al*., Mater. Sci. Engng A **410** 188 (2005).
[28] R.E. Schramm and R.P. Reed, Metall. Trans. A **6** 1345 (1975).
[29] G.B. Olson and C. Morris., Metall. Trans. A **7** 1905 (1976).
[30] H. Fujita and S. Ueda, Acta Metall. **20** 759 (1972).
[31] K.P. Staudhammer, L.E. Murr and S.S. Hecker, Acta Metall. **31** 267 (1983).
[32] C.X. Huang, Y.L. Gao, G. Yang, *et al*., J. Mater. Res. **21** 1687 (2006).
[33] V.M. Segal, Mater. Sci. Engng A **197** 157 (1995).
[34] R.L. Miller, Trans. ASM **61** 592 (1968).
[35] C.G. Lee, S. Kim, B. Song, *et al*., Metall. Mater. Int. **8** 435 (2002).
[36] P.L. Mangonon, Metall. Trans. **1** 1577 (1970).
[37] G.V. Kurdjumov and G. Sachs, Z. Phys. **64** 325 (1930).
[38] J.A. Venables, Phil. Mag. **7** 35 (1962).
[39] C.X. Huang, G. Yang, Y.L. Gao, *et al*., J. Mater. Res. **22** 724 (2007).
[40] K. Wang, N.R. Tao, G. Liu, *et al*., Acta Mater. **54** 5281 (2006).
[41] S. Asgari, E. El-Danaf, S.R. Kalidindi, *et al*., Metall. Mater. Trans. A **28** 1781 (1997).
[42] A. Rohatgi, S.K. Vecchio and T.G. Gray III, Metall. Mater. Trans. A **32** 135 (2001).
[43] F.A. Mohamed, Acta Mater. **51** 4107 (2003).
[44] H.C. Shin, T.K. Ha, W.J. Park, *et al*., Key Engng Mater. **233** 667 (2003).
[45] Z.W. Shan, E.A. Stach, J.M.K. Wiezorek, *et al*., Science **305** 654 (2004).
[46] Y. Ivanisenko, I. Maclaren, X. Sauvage, *et al*., Acta Mater. **54** 1659 (2006).
[47] X. Wu, N. Tao, Y. Hong, *et al*., Acta Mater. **53** 681 (2004).
[48] E. Novillo, D. Hernandez, I. Gutierrz, *et al*., Mater. Sci. Engng A **385** 83 (2004).
[49] D.A. Porter and K.E. Easterling, *Phase Transformation in Metals and Alloys* (Chapman & Hall, London, 1981).